# Numerical investigation of turnkey soliton generation in an organically coated microresonator

Xiaobao Zhang, Hui Luo, Wei Xiong, Xinlin Chen, Xiang Han, Guangzong Xiao [*] and Haining Feng
*College of Advanced Interdisciplinary Studies, National University of Defense Technology, Changsha, Hunan 410073, China*

Kerr soliton frequency-comb generation in microresonators has attracted extensive interest since soliton microcombs offer the potential for integration and can be widely used in many fields, such as spectroscopy, communications, precision metrology, sensing, etc. Here, the mechanism of turnkey soliton generation in a microresonator with an organic material coating is illustrated and investigated in both analytical and numerical ways. In particular, based on the thermal curve under a stable state and soliton power from analytical analysis, the turnkey soliton generation regime is calculated and proved by coupled equations with the split-step Fourier method. In addition, the physical parameters of the hybrid modes in the coated resonators are studied, and a suitable design is given in this paper. This research will be helpful for increasing the accessibility of Kerr solitons and make them easier to integrate.

## I. INTRODUCTION

Soliton microcombs are mode-locked pulse trains generated by continuously pumping a microresonator with Kerr nonlinearity [1]. Promising chip-scale modules [2,3], soliton microcombs have found a remarkable broad range of applications, including time keeping [4,5], spectroscopy [6,7], ranging [8,9], frequency synthesizer [10], and astronomical calibrations [11,12]. To combine the advantage of material optical properties, photonic integration, and compatibility with complementary metal-oxide semiconductor circuits, optical microresonators made from different materials and structures have been intensively studied for soliton microcomb generation [13–20]. However, it is challenging to access the soliton regime due to the thermal effects of the material, which manifest as resonant frequency shifting caused by the temperature increment at a high pump power [21]. As isolated localized structures generated on the red-detuned side of a cavity resonance [22], the thermo-optic effect destabilizes the direct soliton generation process, and a high-power chaotic state is experienced before the soliton-generated [13,22]. Temperature drift induced by the thermo-optic effect pulls the input laser out of the soliton regime, which makes it hard to further capture and stabilize the soliton. This phenomenon is illustrated in Fig. 1. Many techniques have been demonstrated to overcome this issue, for example, power modulation [23], auxiliary lasers [24], fast single-sideband scanning [25], and cryogenic operation [26,27]. Despite the recent development of an injection-locked turnkey soliton microcomb module [3,28], accessing the soliton regime with a regular continuous-wave (cw) laser is still challenging.

Organically coated microresonators have been demonstrated with high quality factors [29,30] and with applications in temperature sensing [31], efficient harmonic generation

[32], and Raman lasers [33]. Featuring a negative thermo-optic coefficient (TOC; $\partial n/\partial T < 0$), organic materials like polydimethylsiloxane (PDMS) and polymethyl methacrylate (PMMA) have been demonstrated to be a reliable coating for the compensation of the general positive TOC [29,34]. In this work, based on the Lugiato-Lefever equation (LLE) [35] coupled with a simplified one-dimensional (1D) thermal diffusion equation, an analytical turnkey soliton microcomb generation regime is investigated with organically coated microresonators. Numerical simulations validate the analytical analysis and demonstrate a turnkey success rate as great as 90%. The design of resonator parameters to access the regime is also investigated with the finite-element method (FEM) for silica wedge [36] and silicon nitride (SiN) ring [15] resonators.

## II. METHODS AND RESULTS

### A. Dynamics of soliton microcombs in an organically coated microresonator

For an organically coated microresonator, the dynamics of a dissipative Kerr soliton in a microresonator is described by the LLE [37],

$$\frac{\partial}{\partial t}A = -\left[\frac{\kappa}{2} + i(\omega_0 - \omega_p) + ig|A|^2 + i\frac{D_2}{2}\frac{\partial^2}{\partial \phi^2}\right]A + \sqrt{\eta\kappa}s_{\text{in}},$$

(1)

where $t$ is time and $\phi$ is the azimuthal angle inside the microresonator. Detuning between cold resonance and pump laser frequency is defined as $\Delta\omega = \omega_0 - \omega_p$. $A$ denotes the optical field, and it is normalized by photon number; therefore, the energy of the field can be expressed as $w = \hbar\omega_0|A|^2$. Similarly, $P_{\text{in}} = \hbar\omega_p|s_{\text{in}}|^2$ is the input cw pump power. $\eta = \kappa_{\text{ext}}/\kappa$ is the coupling efficiency determined by the ratio of the cavity-waveguide coupling loss $\kappa_{\text{ext}}$ to the total resonator loss $\kappa$. The nonlinear coupling coefficient $g$ is
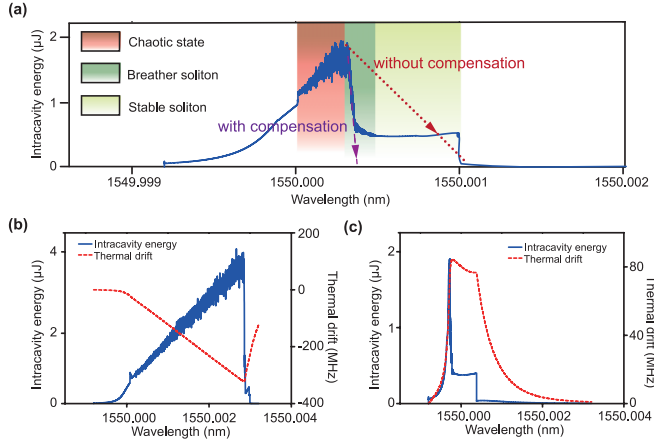
─────────
*xiaoguangzong@nudt.edu.cn

FIG. 1. Influence of the thermo-optic effect on soliton generation. The three panels demonstrate the intracavity energy when the input laser is scanned towards a longer wavelength of silica wedge resonators with a wedge angle of 8° and different coating thicknesses. The design of the silica wedge resonators is given in Sec. II C. The input power is 0.7 W, and the scanning speed is about 1.5 THz/s in all panels. The results are calculated under critical coupling, and the thermal process is amplified 100 times. (a) The PDMS layer thickness is 1200 nm, and the TOC is almost zero. This plot shows the process of soliton generation without the thermo-optic effect. Different states of the process are shaded in different colors (gray scales). The purple dashed line and red dotted line demonstrate the directions of the process move with and without coating compensation, respectively. (b) This silica wedge resonator does not have a PDMS coating, and its TOC is positive. The red dashed line shows the resonance frequency drift caused by the thermo-optic effect. When it comes into the soliton regime, the plunge of the intracavity energy (temperature) causes a positive thermal drift which pulls the input laser out of the soliton regime, and this makes the soliton step become very short. (c) The PDMS layer thickness is 1210 nm, and it suffers a negative thermo-optic effect. The soliton step is slightly extended by the negative thermo-optic effect.

defined as [38]

$$g = \frac{\hbar \omega_0^2 c n_2}{n^2 V_{\text{eff}}}, \qquad (2)$$

where $n$ and $n_2$ are the refractive and nonlinear refractive indexes and $c$ is the speed of light in a vacuum. $V_{\text{eff}}$ denotes the effective volume of the pumped mode. The frequency of the $\mu$th soliton comb line can be approximated with the Taylor expansion.

$$\omega_\mu = \omega_0 + D_1 \mu + \frac{1}{2} D_2 \mu^2 + \sum_{j>2} \frac{1}{j!} D_j \mu^j, \qquad (3)$$

where $D_1$ represents the free spectral range and $D_2$ characterizes the group-velocity dispersion (GVD). The relation between $D_2$ and the GVD ($\beta_2$) can be expressed as $\beta_2 = -n D_2/(c D_1^2)$. A 1D thermal diffusion equation is utilized to describe thermal diffusion process in microresonators, which can be expressed as [39,40]

$$\frac{d \Delta T_t}{dt} = -\kappa_t \Delta T_t + \gamma_t w_e, \qquad (4)$$

where $\Delta T_t$ and $\kappa_t$ are the effective-mode temperature variation and heat dissipation rate, respectively. A detailed definition of $\Delta T_t$ is given in Sec. II C. $\gamma_t$ characterizes the heat source from the optical field, and $w_e$ denotes the average light energy inside the cavity. The two equations can be normalized as

$$\frac{d\psi}{d\tau} = \frac{i}{2} \frac{\partial^2 \psi}{\partial \theta^2} + i|\psi|^2 \psi - (i\zeta + 1)\psi + f, \qquad (5)$$

$$\frac{d\Delta T_t}{dt} = -\kappa_t \Delta T_t + \frac{\Gamma_t}{2\pi} \int |\psi|^2 d\theta, \qquad (6)$$

$$\psi = \sqrt{\frac{2g}{\kappa}} A, \quad \tau = \kappa t/2, \quad \theta = \phi \sqrt{\frac{\kappa}{2D_2}},$$

$$f = \sqrt{\frac{8g\eta P_{\text{in}}}{\kappa^2 \hbar \omega_0}}, \quad \zeta = 2\Delta\omega/\kappa, \quad \Gamma_t = \frac{\hbar \omega_0 \kappa}{2g} \gamma_t.$$

For analytical analysis, a soliton ansatz of the LLE is used [41],

$$\psi(\theta) = \psi_0 + e^{i\varphi} \sum_{i=1}^{N} B \text{sech}\left[\frac{(\theta - \theta_i)}{\tau_\theta}\right], \qquad (7)$$

where $\psi_0$ is a background corresponding to the cw solution of Eq. (5), $B$ is the amplitude of the pulse, $\theta_i$ is the central position of the soliton, $\tau_\theta$ is the pulse width, and $\varphi$ is a phase factor. The overall normalized average intracavity energy is calculated as

$$w_n = \frac{1}{2\pi} \int |\psi|^2 d\theta$$

$$= |\psi_0|^2 + \frac{B\tau_\theta}{\sqrt{\kappa/2D_2}} \text{Re}[\psi_0 e^{-i\varphi}] + \frac{B^2 \tau_\theta}{\pi \sqrt{\kappa/2D_2}}. \qquad (8)$$

$\kappa_t$ and $\Gamma_t$ in Eq. (6) are calculated by FEM in the frequency domain. In the FEM simulations, the optical field is set as the heat source to get the temperature distribution; then it is combined with the mode energy distribution to obtain $\Delta T_t$. In the frequency domain, Eq. (6) can be transformed to

$$\Delta T_t(\omega) = \left| \frac{\Gamma_t w_n}{i\omega + \kappa_t} \right|. \qquad (9)$$

This equation illustrates that $\Delta T_t$ exhibits a Lorentzian spectral response shape. Figure 2 gives the result of the simulation data and fitting curve from Eq. (9). $\kappa_t$ and $\Gamma_t$ derived from these data are about 1019 Hz and 22422 K/s, respectively. The $R^2$ of the fitting curve is about 0.9997, which means the simulation data highly coincide with the theoretical model.

### B. A turnkey soliton generation regime

In this section, a turnkey soliton generation regime is analyzed analytically and simulated numerically. The turnkey process is achieved with the following three stages automatically, as shown in Fig. 3(a). First, the laser is turned on, and intracavity power rises above the parametric oscillation threshold. Second, parametric sidebands are generated, and the temperature rises to push the cavity resonant frequency larger as a result of the negative thermo-optic effect. Overall detuning $\zeta$ sweeps from the blue side to the red side. Third, as overall detuning enters the soliton regime, solitons are generated, and the system stabilizes to a steady soliton solution.
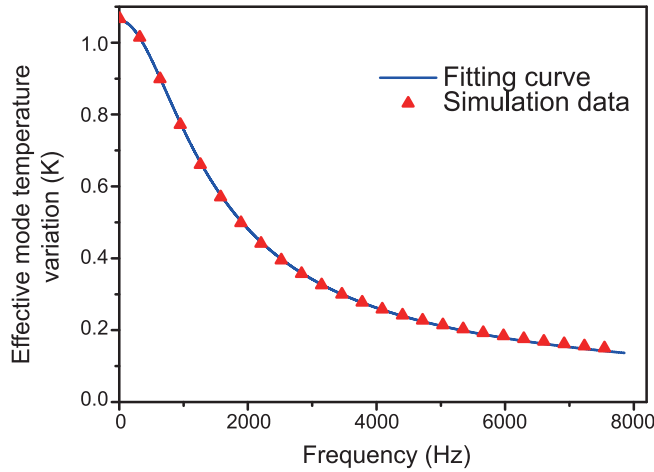
FIG. 2. Simulated frequency response of the thermo-optic effect. This result is acquired by a SiN microresonator with a waveguide width of $0.6\,\mu m$ and a PMMA coating thickness of 280 nm. The design of the SiN ring resonators is given in Sec. II C.

The process takes place automatically after the laser is turned on, and it features the timescale of the thermal relaxation.

With analytic soliton power, the turnkey soliton generation regime is evaluated. There are two requirements to realize the soliton regime. First, after the laser is tuned on, intracavity power must reach the parametric threshold to allow the parametric process. Second, the intersection of the soliton power curve and the thermo-optic curve must be in the soliton regime, so that the final detuning should satisfy [22]

$$\zeta < \frac{\pi^2 f^2}{8}. \tag{10}$$

The calculated pump power $f^2$ with starting laser detuning $\zeta$ (relative to the cold cavity resonance) for turnkey soliton generation is plotted in Fig. 3(c).

To verify the analytical soliton generation regime, simulations based on the split-step Fourier method are utilized. The pump power is fixed at 15, and different starting detunings are chosen. For each detuning, simulations are run 50 times. As the difference in timescale between the LLE ($<1$ ps) and thermal diffusion equation ($\sim 1$ ms) is very large, the thermal process is accelerated 3000 times to reduce computation costs. Namely, $\Gamma_t$ and $\kappa_t$ are amplified 3000 times. In this way, we need to calculate only $1/3000$ the time of the real thermal process equilibrium. Representative switching-on soliton results from 10 consecutive runs are shown in Fig. 3(b). As the nonlinear response due to the Kerr effect is almost instantaneous [40,42], here, the turn-off time is about $2.5\,\mu s$, which is selected by the demand of resetting the thermal effect. It is apparent from the bottom panel in Fig. 3(b) that different soliton numbers acquire their stable state at different detunings, in other words, different thermal drifts. This result is also demonstrated in Fig. 3(a), as the intersections between larger soliton numbers and the thermal curve have larger $\zeta$. Figure 3(d) gives the success rates of the simulated turnkey solitons, and the counts of stabilizing to different soliton numbers according to Fig. 3(d) are plotted in Fig. 3(e).

When $f^2 = 15$, the pump detuning range set by the parametric threshold is $-2.74 < \zeta < 4.74$. In Figs. 3(d) and 3(e), the calculated detuning is from $-3$ to 5 with an interval of 0.5. As the breather solitons are not stable [43], they are not regarded as successful turnkey solitons and are expelled from success rates as well as the counts of soliton numbers in Fig. 3(e). The results show good coherence with the calculated turnkey soliton generation regime. When $\zeta = 5$, detuning is larger than the upper limit, and the success rate is zero. As $\zeta$ decreases, which means the thermo-optic curve shifts to the right, the smaller soliton numbers (small $N$) first reach their thermal equilibrium in the breather soliton regime, which causes small soliton numbers to disappear. The soliton numbers $N = 1, 2, 3$ transform to breather solitons at $\zeta = 3, 0.5, -1.5$, respectively. This phenomenon is also obvious in Fig. 3(e); while $\zeta$ decreases, the counts of small soliton numbers disappear as they become breather solitons, and larger soliton numbers start to appear because they begin to intersect with the thermal curve. The highest success rate (90%) appears at $\zeta = 1$, as this detuning can support three different soliton numbers, which is similar to the detuning range from 3.5 to 4.5 and $\zeta = 1.5$. However, under this parameter setting, it seems that soliton numbers 3 and 4 have higher generation rates than those of 1 and 2, and this phenomenon pulls the success rate of $\zeta = 1$ to the highest one. The difference in success rates between $\zeta = 1$ and $\zeta = 1.5$ should be from statistical problems. When $\zeta = -3$, it exceeds the lower limit of the threshold power, and the success rate reduces to zero.

### C. Design of microresonator parameters to access this regime

Numeric modeling requires detailed information about the microresonator parameters. In this section, the parameters are taken from the literature or derived from theory. The mode energy distribution of the organically coated microresonators is calculated by FEM. In the coated microresonators, light propagates in both the resonator materials and organic coatings as the relatively small contrast in refractive indexes between them. The effective refractive index of the hybrid whispering-gallery mode (WGM) can be expressed as

$$n_{\text{eff}} \approx \sum_i \eta_i n_i \quad (i = 1, 2, 3, \dots), \tag{11}$$

where $\eta_i$ represents the fractions of light energy traveling in the different materials and the sum of $\eta_i$ is 1. $n_i$ denotes the refractive index of the medium. Similarly, the effective TOC of the hybrid WGM appears as [29]

$$\frac{dn_{\text{eff}}}{dT} \approx \sum_i \eta_i \frac{dn_i}{dT} \quad (i = 1, 2, 3, \dots). \tag{12}$$

In addition to the effective refractive index and effective TOC, the effective-mode temperature variation $\Delta T_t$ is also relative to the mode energy distribution. In microcavities, the heat is from the material absorption of the optical energy, and it transfers from the mode volume to the entire wafer. Particularly, it is the temperature of the mode volume that mainly determines the influence of the thermo-optic effect. Hence, $\Delta T_t$ is defined as the temperature difference between the wafer temperature and the quasiequilibrium one weighted by the intensity distribution of the mode. The expression of $\Delta T_t$ is
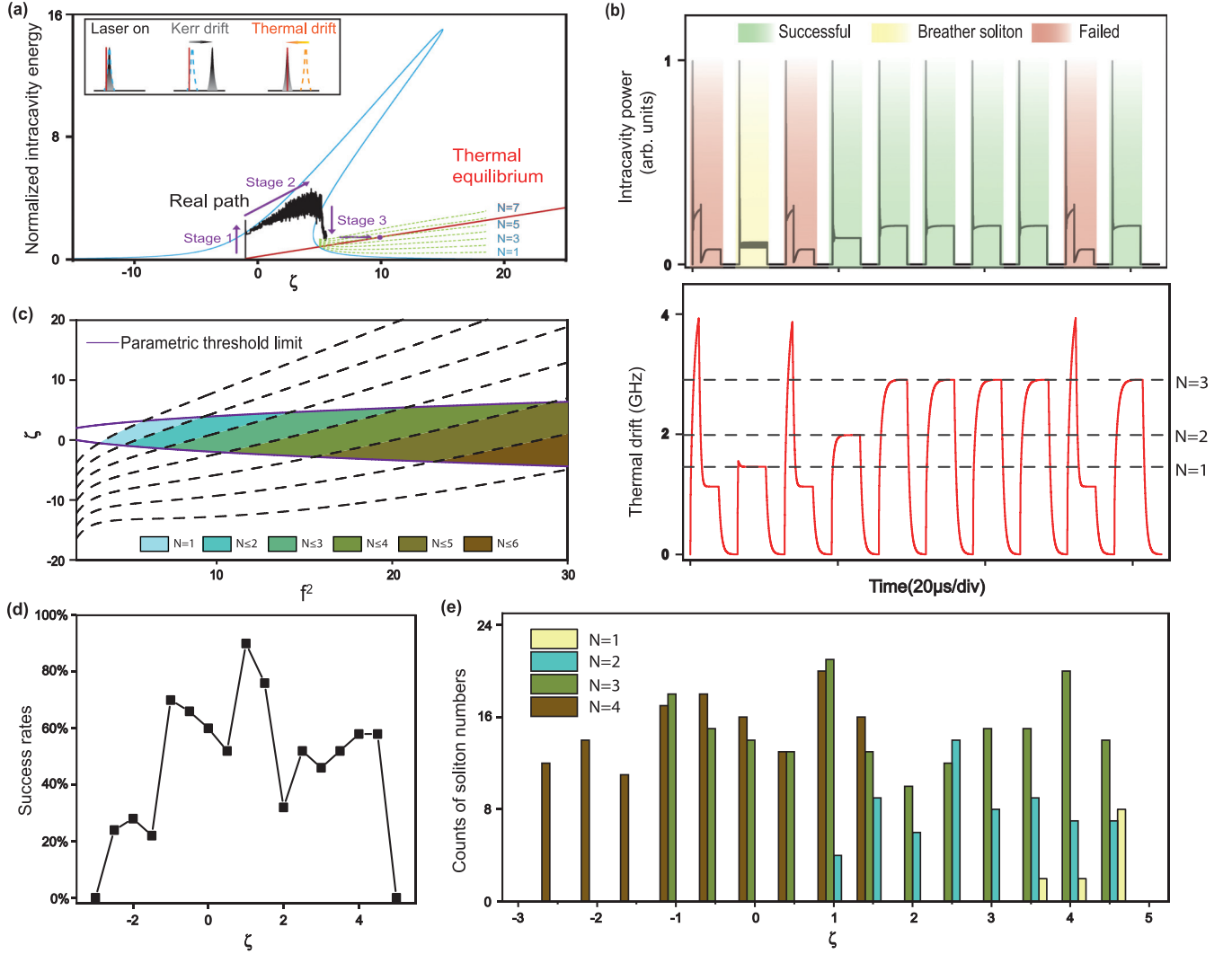
FIG. 3. Turnkey soliton generation. The turnkey solitons are generated in a SiN ring resonator which is designed in Sec. II C. The width of the SiN is $0.6\,\mu$m, and the PMMA coating thickness is 275 nm. (a) Process of an automatically generated soliton. The inset illustrates the mechanism of the transition to the soliton state, and the blue (light gray) line demonstrates the bistability caused by the Kerr nonlinearity. The black line is acquired from the numerical calculation of the LLE, and it shows the real path of the self-start soliton generation in the simulation. The red (dark gray) line is the thermo-optic curve which is derived from Eq. (6) when it reaches the steady state. Intersections of the red (dark gray) line and soliton steps (dashed lines) mean these soliton numbers can reach the thermal equilibrium. (b) Representative switching-on soliton results from 10 consecutive runs. The bottom panel shows the corresponding thermal drift according to the top panel. Detuning $\zeta$ is 2.5. The ones which are failed to generate solitons do not have intersections with the thermo-optic curve. Their soliton power is too high, and the thermal drift pulls them out of the soliton regime. The breather soliton means the intersections are in the breather soliton regime. Namely, the soliton number $N$ is too small. (c) Calculated turnkey soliton generation regime. The black dashed lines are set by the different soliton numbers. The parametric threshold has upper and lower detuning limits for a determined input power as there are two detunings for one determined intracavity power. (d) Success rates of different pump detunings when $f^2 = 15$. Every detuning is calculated 50 times. (e) The counts of stabilizing to different soliton numbers in (d).

given by

$$\Delta T_t = \frac{\sum_i \varepsilon_i \iiint_v |\Delta T| |E|^2 dv}{\sum_i \varepsilon_i \iiint_v |E|^2 dv}, \tag{13}$$

where $\varepsilon_i$, $\Delta T$, and $E$ are the permittivity, temperature variation, and electric-field intensity, respectively. Different from the effective refractive index and effective TOC, the effective nonlinear refractive index $n_{2,\mathrm{eff}}$ of a hybrid mode is determined by the biquadrate of the electric-field intensity

inside the materials. Therefore, the effective nonlinear refractive index appears [44]:

$$n_{2,\mathrm{eff}} \approx \sum_i \eta_i{}' n_{2,i} \quad (i = 1, 2, 3, \ldots), \tag{14}$$

$$\eta_i{}' = \frac{\varepsilon_i \iint_{s_i} |E|^4 ds}{\sum_i \varepsilon_i \iint_{s_i} |E|^4 ds}. \tag{15}$$

In addition, the coatings also have a large influence on the quality factors $Q$ of WGMs as the light absorption coefficient of different materials varies. The intrinsic $Q$ ($Q_{\mathrm{int}}$) of a WGM

TABLE I. Parameters of different materials used in the simulation.

|  | SiO$_2$ | Si$_3$N$_4$ | PDMS | PMMA |
|---|---|---|---|---|
| $n$ | 1.4440 | 1.9744 | 1.4039 | 1.4809 |
| $n_2$ (m$^2$/W) | $3\times10^{-20}$ | $2.5\times10^{-19}$ | $2.8\times10^{-18}$ | $1.1\times10^{-18}$ |
| $dn/dt$ (K$^{-1}$) | $1.19\times10^{-5}$ | $2.45\times10^{-5}$ | $-1.00\times10^{-4}$ | $-1.04\times10^{-4}$ |
| $\alpha$ (m$^{-1}$) | 0.0156 | 0.243 | 2.30 | 20.3 |
| $\beta_2$ (fs$^2$/mm) | $-27.947$ | 8.374 | 17.122 | $-25.918$ |

is mainly determined by absorption $Q$ ($Q_{\text{abs}}$) and scattering $Q$ ($Q_{\text{sca}}$):

$$\frac{1}{Q_{\text{int}}} = \frac{1}{Q_{\text{abs}}} + \frac{1}{Q_{\text{sca}}}. \tag{16}$$

In the calculations, we assume the coatings change only $Q_{\text{abs}}$, and it can be written as

$$Q_{\text{abs}} = \omega \frac{T_{rt}}{\sum_i \eta_i (1 - e^{-\alpha_i L})}, \tag{17}$$

where $\omega$, $\alpha_i$, $T_{rt}$, and $L$ denote the laser frequency, linear absorption coefficient, round-trip time, and round-trip length, respectively. To generate soliton Kerr frequency combs, the GVD of the modes must be controlled in the anomalous dispersion regime [45]. Namely, $D_2$ must be kept positive. Numerical modeling of the WGM's GVD is also realized by the FEM. The geometry and GVD of the materials both impact the WGM's GVD. In the design, because materials we used are definite, the dispersion engineering is mainly determined by the geometric parameters. Another important parameter is the parametric threshold power. It should be at a reasonable level to ensure the soliton combs can be generated in practical experiments. The input threshold power $P_{\text{th}}$ of hybrid modes is given by [14,45,46]

$$P_{\text{th}} = \frac{\pi n_{\text{eff}} \omega_0 A_{\text{eff}}}{4\eta n_{2,\text{eff}}} \frac{1}{D_1 Q_{\text{tot}}^2}, \tag{18}$$

where $A_{\text{eff}}$ is the effective-mode area and it is calculated by FEM. $Q_{\text{tot}}$ represents the $Q$ factor which includes both intrinsic and coupling loss. In this paper, critical coupling is used in all calculations, which means $\eta = 1/2$ and $Q_{\text{tot}} = Q_{\text{int}}/2$.

Table I gives the parameters around 1550 nm used in the design. The absorption coefficient of SiN is obtained by calculating the effective-mode temperature variation by FEM combined with the thermal drift of the resonance measured from experiments. The other parameters are obtained from Refs. [47–52].

Simulation results show that using PDMS as the coating material improves the performance of silica wedge resonators, which possess the advantage of a high $Q$ factor. Compared to PMMA, PDMS has a smaller absorption coefficient, which induces less influence on its $Q$ factor. In addition, the refractive index of PDMS is smaller than that of silica, which can ensure less mode energy is distributed in the thin PDMS coatings. For geometry, $D_2$ decreases with the increase of the PDMS coating thickness and the decrease of the wedge angle. However, larger wedge angles need thicker coatings to compensate for the thermal effect. In order to balance thermal compensation and $D_2$, in the simulations, it is found that only small wedge angles can both compensate for the thermal effect and have a positive $D_2$. The diameter of the resonators mainly influences

$D_1$ and $D_2$; however, it works as a multiplier to magnify or minify $D_2$ at different diameters and can hardly invert the sign of $D_2$. The thickness of the silica disk has a tiny influence on $D_2$ and the energy distribution of the modes compared with wedge angles. Therefore, the wedge angle is regarded as a variable for the design. Figure 4 shows the results of the designed PDMS-coated wedge resonators with different wedge angles. The diameter of the designed resonators is 3 mm with a silica disk thickness of 8 $\mu$m according to general silica wedge resonators [36].

Different from silica resonators, PMMA is used to coat the SiN ring resonators. The refractive index difference between SiN and PDMS is larger than that between SiN and PMMA, which means that thicker coatings are required to compensate for the positive thermo-optic effect when PDMS instead of PMMA is employed as the coating material. Moreover, the GVD of PMMA is negative; both of the refractive index difference and GVD of the material PMMA coatings much easier to balance the thermal compensation and dispersion. Actually, in the simulations, we did not find suitable parameters for a PDMS-coated SiN ring resonator. For a general SiN ring resonator, SiN is inlaid in a silica-based material [48].
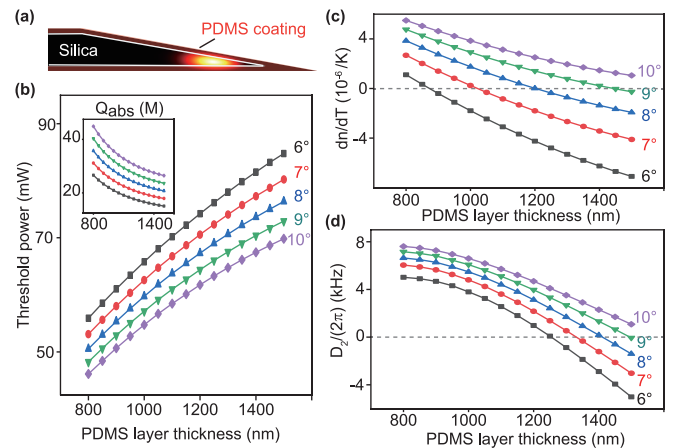


FIG. 4. Results of designed PDMS-coated silica wedge resonators. (a) Geometry and mode energy distribution of the designed silica resonators. The energy distribution in the air is neglected since it is too small. In the simulations, the PDMS coatings are assumed to cover the silica evenly on all surfaces. The diameter and the thickness are included only for silica. (b) Threshold power of the designed silica resonators with different wedge angles. The inset shows the absorption $Q$, and the scattering $Q$ is set as 100 million in the calculations. (c) TOC of the designed silica resonators with different wedge angles. (d) $D_2/2\pi$ of the designed silica resonators with different wedge angles.
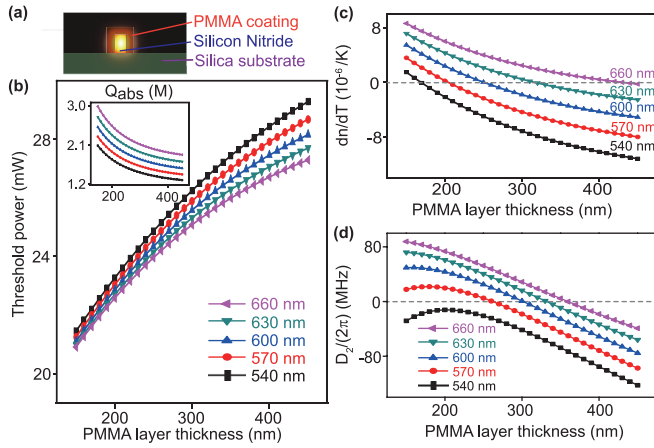
FIG. 5. Results of designed PMMA-coated SiN ring resonators. (a) Geometry and mode energy distribution of the designed SiN resonators. (b) Threshold power of the designed SiN resonators with different widths. The inset shows the absorption $Q$, and the scattering $Q$ is set as 1 million in the calculations. (c) TOC of the designed SiN resonators with different widths. (d) $D_2/2\pi$ of the designed SiN resonators with different widths.

In our design, the top and side of the SiN is coated with a PMMA layer of the same thickness, while silica is used as the substance to adhere to the SiN. The width and the height of the SiN have interchangeability in the design; therefore, the width is chosen as the variable for demonstration. The results for PMMA-coated SiN ring resonators with different widths are shown in Fig. 5. The diameter of the designed ring resonators is 88 $\mu$m, and the height of the SiN is 1 $\mu$m.

### III. DISCUSSION

Thermal noise is ubiquitous in microresonator systems of Kerr solitons. Previous studies revealed how thermal fluctuations lead to the phase noise in soliton microcombs [24,25]. A distribution of measurement results for $f_{\rm rep}$, which denotes the repetition frequency of a soliton circulating in a microresonator, can be used to characterize the phase noise. The tuning of $f_{\rm rep}$ with temperature $T$ is given by [24]

$$\frac{df_{\rm rep}}{dT} = \frac{f_{\rm rep}}{n}\left(\frac{\partial n}{\partial T} + \frac{\partial n}{\partial \omega_s}\frac{\partial \omega_s}{\partial \Delta\omega}\frac{\partial \Delta\omega}{\partial T}\right), \qquad (19)$$

where $\omega_s$ is the soliton carrier frequency. This equation illustrates that the phase noise caused by thermal fluctuations is affected by the TOC ($\partial n/\partial T$), dispersion ($\partial n/\partial \omega_s$),

soliton-frequency-shift tuning ($\partial\omega_s/\partial\Delta\omega$), and thermal tuning ($\partial\Delta\omega/\partial T$). Here, the PMMA-coated SiN resonator demonstrated for the turnkey soliton generation has a dispersion similar to that of the general SiN resonators for soliton generation. The soliton-frequency-shift tuning is mainly determined by the Raman effect and interactions between modes which are not considered in this paper [53]. However, the absolute value of the TOC of the hybrid mode ($-1.15\times10^{-6}$) is an order of magnitude lower than that of SiN, which leads to smaller absolute values of $\partial n/\partial T$ and $\partial\Delta\omega/\partial T$ in Eq. (19). Therefore, the thermal decoherence in soliton microcombs may be alleviated by this coating design.

The method developed in this paper can be applied in soliton-comb generation of any hybrid modes with different materials considering the thermal effect. It is believed the success rate could be higher when changing the different pump powers or the thickness of the coating. However, as there is not an analytical method to get the breather soliton regime and the suitable generation regime is a balance of dispersion, $Q$, the TOC, and thermal parameters, which require a huge amount of computation, accurate suitable coating thickness ranges for turnkey soliton generation are unknown [43]. Here, based on the coating thickness we have tried, the suitable coating thickness ranges for silica wedge resonators with a wedge angle of $8°$ and SiN ring resonators with a width of $0.6\,\mu$m are at least 100 and 20 nm, respectively.

### IV. CONCLUSION

In summary, we have numerically investigated turnkey soliton generation in a PMMA-coated SiN ring resonator. The calculations show that the designed coated resonator can generate turnkey solitons at a high success rate of 90% when the normalized pump power is 15. The model we developed for calculating the turnkey soliton generation regime meets the results obtained from numerical methods based on the LLE combined with the thermal diffusion equation. In addition, the FEM simulation we set for calculating thermal parameters highly coincides with the theoretical model. Finally, we investigated the physical parameters of hybrid modes in coated microresonators, and a model for organically coated microresonator parameter design was established. It illustrates PDMS-coated silica wedge resonators and PMMA-coated SiN ring resonators can realize the turnkey soliton generation automatically without scanning the pump laser, which can greatly increase the accessibility of soliton combs and makes them easier to integrate.

[1] T. J. Kippenberg, A. L. Gaeta, M. Lipson, and M. L. Gorodetsky, Dissipative Kerr solitons in optical microresonators, Science **361**, 567 (2018).

[2] B. Stern, X. Ji, Y. Okawachi, A. L. Gaeta, and M. Lipson, Battery-operated integrated frequency comb generator, Nature (London) **562**, 401 (2018).

[3] B. Shen, L. Chang, J. Liu, H. Wang, Q.-F. Yang, C. Xiang, R. N. Wang, J. He, T. Liu, W. Xie, J. Guo, D. Kinghorn, L. Wu,

Q.-X. Ji, T. J. Kippenberg, K. Vahala, and J. E. Bowers, Integrated turnkey soliton microcombs, Nature (London) **582**, 365 (2020).

[4] S. B. Papp, K. Beha, P. Del'Haye, F. Quinlan, H. Lee, K. J. Vahala, and S. A. Diddams, Microresonator frequency comb optical clock, Optica **1**, 10 (2014).

[5] Z. L. Newman *et al.*, Architecture for the photonic integration of an optical atomic clock, Optica **6**, 680 (2019).

[6] M.-G. Suh, Q.-F. Yang, K. Y. Yang, X. Yi, and K. J. Vahala, Microresonator soliton dual-comb spectroscopy, Science **354**, 600 (2016).

[7] Q.-F. Yang, B. Shen, H. Wang, M. Tran, Z. Zhang, K. Y. Yang, L. Wu, C. Bao, J. Bowers, A. Yariv, and K. Vahala, Vernier spectrometer using counterpropagating soliton microcombs, Science **363**, 965 (2019).

[8] M.-G. Suh and K. J. Vahala, Soliton microcomb range measurement, Science **359**, 884 (2018).

[9] P. Trocha, M. Karpov, D. Ganin, M. H. P. Pfeiffer, A. Kordts, S. Wolf, J. Krockenberger, P. Marin-Palomo, C. Weimann, S. Randel, W. Freude, T. J. Kippenberg, and C. Koos, Ultrafast optical ranging using microresonator soliton frequency combs, Science **359**, 887 (2018).

[10] D. T. Spencer *et al.*, An optical-frequency synthesizer using integrated photonics, Nature (London) **557**, 81 (2018).

[11] M.-G. Suh, X. Yi, Y.-H. Lai, S. Leifer, I. S. Grudinin, G. Vasisht, E. C. Martin, M. P. Fitzgerald, G. Doppmann, J. Wang, D. Mawet, S. B. Papp, S. A. Diddams, C. Beichman, and K. Vahala, Searching for exoplanets using a microresonator astrocomb, Nat. Photon. **13**, 25 (2019).

[12] E. Obrzud, M. Rainer, A. Harutyunyan, M. H. Anderson, J. Liu, M. Geiselmann, B. Chazelas, S. Kundermann, S. Lecomte, M. Cecconi, A. Ghedina, E. Molinari, F. Pepe, F. Wildi, F. Bouchy, T. J. Kippenberg, and T. Herr, A microphotonic astrocomb, Nat. Photon. **13**, 31 (2019).

[13] T. Herr, V. Brasch, J. D. Jost, C. Y. Wang, N. M. Kondratiev, M. L. Gorodetsky, and T. J. Kippenberg, Temporal solitons in optical microresonators, Nat. Photon. **8**, 145 (2014).

[14] X. Yi, Q.-F. Yang, K. Y. Yang, M.-G. Suh, and K. Vahala, Soliton frequency comb at microwave rates in a high-Q silica microresonator, Optica **2**, 1078 (2015).

[15] V. Brasch, M. Geiselmann, T. Herr, G. Lihachev, M. H. P. Pfeiffer, M. L. Gorodetsky, and T. J. Kippenberg, Photonic chip–based optical frequency comb using soliton Cherenkov radiation, Science **351**, 357 (2016).

[16] T. Kobatake, T. Kato, H. Itobe, Y. Nakagawa, and T. Tanabe, Thermal effects on Kerr comb generation in a $CaF_2$ whispering-gallery mode microcavity, IEEE Photon. J. **8**, 1 (2016).

[17] B. Yao, S. W. Huang, Y. Liu, A. K. Vinod, C. Choi, M. Hoff, Y. Li, M. Yu, Z. Feng, D. L. Kwong, Y. Huang, Y. Rao, X. Duan, and C. W. Wong, Gate-tunable frequency combs in graphene-nitride microresonators, Nature (London) **558**, 410 (2018).

[18] Y. He, Q.-F. Yang, J. Ling, R. Luo, H. Liang, M. Li, B. Shen, H. Wang, K. Vahala, and Q. Lin, Self-starting bi-chromatic $LiNbO_3$ soliton microcomb, Optica **6**, 1138 (2019).

[19] J. Liu, E. Lucas, A. S. Raja, J. He, J. Riemensberger, R. N. Wang, M. Karpov, H. Guo, R. Bouchand, and T. J. Kippenberg, Photonic microwave generation in the X- and K-band using integrated soliton microcombs, Nat. Photon. **14**, 486 (2020).

[20] H.-J. Chen, Q.-X. Ji, H. Wang, Q.-F. Yang, Q.-T. Cao, Q. Gong, X. Yi, and Y.-F. Xiao, Chaos-assisted two-octave-spanning microcombs, Nat. Commun. **11**, 2336 (2020).

[21] T. Carmon, L. Yang, and K. Vahala, Dynamical thermal behavior and thermal self-stability of microcavities, Opt. Express **12**, 4742 (2004).

[22] H. Guo, M. Karpov, E. Lucas, A. Kordts, M. H. P. Pfeiffer, V. Brasch, G. Lihachev, V. E. Lobanov, M. L. Gorodetsky, and T. J. Kippenberg, Universal dynamics and deterministic switch-ing of dissipative Kerr solitons in optical microresonators, Nat. Phys. **13**, 94 (2016).

[23] X. Yi, Q.-F. Yang, K. Youl, and K. Vahala, Active capture and stabilization of temporal solitons in microresonators, Opt. Lett. **41**, 2037 (2016).

[24] T. E. Drake, J. R. Stone, T. C. Briles, and S. B. Papp, Thermal decoherence and laser cooling of Kerr microresonator solitons, Nat. Photon. **14**, 480 (2020).

[25] J. R. Stone, T. C. Briles, T. E. Drake, D. T. Spencer, D. R. Carlson, S. A. Diddams, and S. B. Papp, Thermal and Non-linear Dissipative-Soliton Dynamics in Kerr-Microresonator Frequency Combs, Phys. Rev. Lett. **121**, 063902 (2018).

[26] G. Moille, X. Lu, A. Rao, Q. Li, D. A. Westly, L. Ranzani, S. B. Papp, M. Soltani, and K. Srinivasan, Kerr-Microresonator Soliton Frequency Combs at Cryogenic Temperatures, Phys. Rev. Appl. **12**, 34057 (2019).

[27] G. Moille, L. Chang, W. Xie, A. Rao, X. Lu, M. Davanco, J. E. Bowers, and K. Srinivasan, Dissipative Kerr solitons in a III-V microresonator, Laser Photon. Rev. **14**, 2000022 (2020).

[28] A. S. Voloshin, N. M. Kondratiev, G. V. Lihachev, J. Liu, V. E. Lobanov, N. Y. Dmitriev, W. Weng, T. J. Kippenberg, and I. A. Bilenko, Dynamics of soliton self-injection locking in optical microresonators, Nat. Commun. **12**, 235 (2021).

[29] L. He, Y.-F. Xiao, C. Dong, J. Zhu, V. Gaddam, and L. Yang, Compensation of thermal refraction effect in high-Q toroidal microresonator by polydimethylsiloxane coating, Appl. Phys. Lett. **93**, 201102 (2008).

[30] H. S. Choi, X. Zhang, and A. M. Armani, Hybrid silica-polymer ultra-high-Q microresonators, Opt. Lett. **35**, 459 (2010).

[31] C.-H. Dong, L. He, Y.-F. Xiao, V. R. Gaddam, S. K. Ozdemir, Z.-F. Han, G.-C. Guo, and L. Yang, Fabrication of high-Q polydimethylsiloxane optical microspheres for thermal sensing, Appl. Phys. Lett. **94**, 231119 (2009).

[32] J.-H. Chen, X. Shen, S.-J. Tang, Q.-T. Cao, Q. Gong, and Y.-F. Xiao, Microcavity Nonlinear Optics with an Organically Functionalized Surface, Phys. Rev. Lett. **123**, 173902 (2019).

[33] X. Shen, H. Choi, D. Chen, W. Zhao, and A. M. Armani, Raman laser from an optical resonator with a grafted single-molecule monolayer, Nat. Photonics **14**, 95 (2020).

[34] H. S. Choi and A. M. Armani, Thermal nonlinear effects in hybrid optical microresonators, Appl. Phys. Lett. **97**, 223306 (2010).

[35] L. A. Lugiato and R. Lefever, Spatial Dissipative Structures in Passive Optical Systems, Phys. Rev. Lett. **58**, 2209 (1987).

[36] H. Lee, T. Chen, J. Li, K. Y. Yang, S. Jeon, O. Painter, and K. J. Vahala, Chemically etched ultrahigh-Q wedge-resonator on a silicon chip, Nat. Photon. **6**, 369 (2012).

[37] A. B. Matsko, A. A. Savchenkov, W. Liang, V. S. Ilchenko, D. Seidel, and L. Maleki, Mode-locked Kerr frequency combs, Opt. Lett. **36**, 2845 (2011).

[38] A. B. Matsko, A. A. Savchenkov, D. Strekalov, V. S. Ilchenko, and L. Maleki, Optical hyperparametric oscillations in a whispering-gallery-mode resonator: Threshold and phase dif-fusion, Phys. Rev. A **71**, 033804 (2005).

[39] M. L. Gorodetsky, A. A. Savchenkov, V. S. Ilchenko, A. V. Kudryashov, and P. Galarneau, Optical microsphere resonators: Optimal coupling to high-Q whispering-gallery modes, J. Opt. Soc. Am. B **16**, 147 (1999).

[40] C. Schmidt, A. Chipouline, T. Pertsch, A. Tünnermann, O. Egorov, F. Lederer, and L. Deych, Nonlinear thermal effects in

optical microspheres at different wavelength sweeping speeds, Opt. Express **16**, 6285 (2008).

[41] X. Li, B. Shen, H. Wang, K. Yang, X. Yi, Q. Yang, and Z. Zhou, Universal iso-contours for dissipative Kerr solitons, Opt. Lett. **43**, 1 (2018).

[42] H. Rokhsari and K. J. Vahala, Observation of Kerr nonlinearity in microcavities at room temperature, Opt. Lett. **30**, 427 (2005).

[43] M. Yu, J. K. Jang, Y. Okawachi, A. G. Griffith, K. Luke, and S. A. Miller, Breather soliton dynamics in microresonators, Nat. Commun. **8**, 14569 (2017).

[44] T. J. Kippenberg, Nonlinear optics in ultra-high-Q whispering-gallery optical microcavities, Ph.D. thesis, California Institute of Technology, 2004.

[45] T. J. Kippenberg, S. M. Spillane, and K. J. Vahala, Kerr-Nonlinearity Optical Parametric Oscillation in an Ultrahigh-$Q$ Toroid Microcavity, Phys. Rev. Lett. **93**, 083904 (2004).

[46] J. Li, H. Lee, T. Chen, and K. J. Vahala, Low-Pump-Power, Low-Phase-Noise, and Microwave to Millimeter-Wave Repetition Rate Operation in Microcombs, Phys. Rev. Lett. **109**, 233901 (2012).

[47] L. Chang, W. Xie, H. Shu, Q.-F. Yang, B. Shen, A. Boes, J. D. Peters, W. Jin, C. Xiang, S. Liu, G. Moille, S.-P. Yu, X. Wang,

K. Srinivasan, S. B. Papp, K. Vahala, and J. E. Bowers, Ultra-efficient frequency comb generation in AlGaAs-on-insulator microresonators, Nat. Commun. **11**, 1331 (2020).

[48] K. Luke, Y. Okawachi, M. R. E. Lamont, A. L. Gaeta, and M. Lipson, Broadband mid-infrared frequency comb generation in a $Si_3N_4$ microresonator, Opt. Lett. **40**, 4823 (2015).

[49] M. J. Weber, *Handbook of Optical Materials* (CRC Press, Boca Raton, FL, 2003).

[50] F. D'Amore, M. Lanata, S. M. Pietralunga, M. C. Gallazzi, and G. Zerbi, Enhancement of PMMA nonlinear optical properties by means of a quinoid molecule, Opt. Mater. (Amsterdam, Neth.) **24**, 661 (2014).

[51] T. Roychowdhury, D. Shah, J. N. Hilfiker, and M. R. Linford, Polymethyl methacrylate: Optical properties from 191 to 1688 nm (0.735–6.491 eV) by spectroscopic ellipsometry, Surf. Sci. Spectra **27**, 016002 (2020).

[52] G. Panusa, Y. E. Pu, J. Wang, C. Moser, and D. Psaltis, Enhancement of PMMA nonlinear optical properties by means of a quinoid molecule, Opt. Mater. Express **9**, 128 (2019).

[53] X. Yi, Q.-F. Yang, X. Zhang, K. Y. Yang, X. Li, and K. Vahala, Single-mode dispersive waves and soliton microcomb dynamics, Nat. Commun. **8**, 14869 (2017).